Rasmussen, Morten K.; Foster, Adam S.; F. Canova, Filippo; Hinnemann, Berit; Helveg, Stig; Meinander, Kristoffer; Besenbacher, Flemming; Lauritsen, Jeppe V.

Noncontact atomic force microscopy imaging of the atomic structure and cation defects of the polar MgAl2O4 (100) surface : Experiments and first-principles simulations

Published in:
Physical Review B

DOI:
10.1103/PhysRevB.84.235419

Published: 01/01/2011

Document Version
Publisher's PDF, also known as Version of record

Please cite the original version:
Rasmussen, M. K., Foster, A. S., F. Canova, F., Hinnemann, B., Helveg, S., Meinander, K., Besenbacher, F., & Lauritsen, J. V. (2011). Noncontact atomic force microscopy imaging of the atomic structure and cation defects of the polar MgAl2O4 (100) surface : Experiments and first-principles simulations. *Physical Review B*, *84*(23), 1-14. Article 235419. https://doi.org/10.1103/PhysRevB.84.235419

Noncontact atomic force microscopy imaging of atomic structure and cation defects of the polar $MgAl_2O_4$ (100) surface: Experiments and first-principles simulations

Morten K. Rasmussen,[1] Adam S. Foster,[2,3] Filippo F. Canova,[2,3] Berit Hinnemann,[4] Stig Helveg,[4] Kristoffer Meinander,[1] Flemming Besenbacher,[1] and Jeppe V. Lauritsen[1,*]

[1]*Interdisciplinary Nanoscience Center (iNANO), University of Aarhus, Denmark*

[2]*Department of Physics, Tampere University of Technology, Finland*

[3]*Department of Applied Physics, Aalto University School of Science, Finland*

[4]*Haldor Topsøe A/S, Nymøllevej 55, 2800 Kongens Lyngby, Denmark*

(Received 16 September 2011; revised manuscript received 30 October 2011; published 2 December 2011)

Atom-resolved noncontact atomic force microscopy (NC-AFM) was recently used to reveal that the insulating spinel $MgAl_2O_4$(100) surface, when prepared under vacuum conditions, adopts a structurally well-defined Al and O-rich structure (Al_4-O_4-Al_4 termination) consisting of alternating Al and double-O rows, which are, however, interrupted by defects identified as interchanged Mg in the surface layers (so-called antisite defects). From an interplay of futher NC-AFM experiments and first-principles NC-AFM image simulations, we present here a detailed analysis of the NC-AFM contrast on the $MgAl_2O_4$(100) surface. Experiments show that the contrast on $MgAl_2O_4$(100) in atom-resolved NC-AFM is dominated by two distinctly different types of contrast modes, reflecting two oppositely charged tip-apex terminations. In this paper, we analyze the contrast associated with these imaging modes and show that a positively charged tip-apex (presumably Mg^{2+}) interacts most strongly with the oxygen atoms, thus imaging the oxygen lattice, whereas a negatively charged tip-apex (O^{2-}) will reveal the cation sublattice on $MgAl_2O_4$. The analysis of force-vs-distance calculations for the two tips shows that this qualitative picture, developed in our previous study, holds for all realistic tip-surface imaging parameters, but the detailed resolution on the O double rows and Al rows changes as a function of tip-surface distance, which is also observed experimentally. We also provide an analysis of the tip dependency and tip-surface distance dependency for the NC-AFM contrast associated with single Al vacancies and Mg-Al antisite defects on the $MgAl_2O_4$(100) surface and show that it is possible on the basis of NC-AFM image simulations to discriminate between the Al^{3+} and Mg^{2+} species in antisite defects and hypothetical Al vacancies.

DOI: 10.1103/PhysRevB.84.235419 PACS number(s): 68.47.Gh, 68.37.Ps

I. INTRODUCTION

Metal oxides adopting the spinel structure are among the most common minerals and a major component of the Earth's upper mantle.[1] Metal oxide spinel minerals are also widely used industrially in ceramics technology and materials science, for instance, as membranes in solid oxide fuel cells[2] and in heterogeneous catalysis, either as refractory porous supports for active metal nanoclusters[2–4] or as catalysts in their own right.[4–6] Resolving the atomic-scale surface structure of insulating spinel metal oxides has in general been extremely challenging, and only recently it was possible to provide insight on the detailed atomic structure of the prototypical system, $MgAl_2O_4$.[7] Magnesium aluminate ($MgAl_2O_4$) is a ternary metal oxide with the spinel crystal structure, which defines a larger group of so-called spinel minerals, with the general formula $A^{2+}B_2{}^{3+}O_4{}^{2-}$.[8,9] Most previous results addressing the issue of surface structure were based on theory,[10–15] and only a very few experimental studies have been presented. Yanina *et al.* used contact mode atomic force microscopy to investigate the stages of surface faceting and coarsening of $MgAl_2O_4$(100) samples exposed to very high temperatures.[14,16] Using low-energy ion scattering (LEIS), van der Laag *et al.* investigated the relative amount of Mg and Al atoms in the surface layer of cleaved $MgAl_2O_4$(100) and compared those findings with DFT simulations to show that fractured surfaces expose a surplus of Mg, reflecting an Mg-terminated surface. Atomic force microscopy (AFM) studies operated in the so-called noncontact mode (NC-AFM) have recently been successfully employed for atomic-scale studies of a range of clean metal oxide insulating surfaces,[17–19] such as α-Al_2O_3(0001)[20–22] or MgO.[23,24] Very recently, we used NC-AFM to resolve the atomic-scale surface structure of the $MgAl_2O_4$(100) surface.[7] The studies in Ref. 7 used an interplay of NC-AFM imaging with surface x-ray diffraction (SXRD) and DFT calculations, revealing that the $MgAl_2O_4$(100) surface under typical O_2 and H_2 containing conditions adopts an Al and O surface termination with a thermodynamically favored amount of Al atoms interchanged with Mg at the surface. As an extension of these studies, we present here a thorough and comprehensive study of the NC-AFM contrast formation on $MgAl_2O_4$(100) based on NC-AFM experiments and DFT-based NC-AFM simulations of $MgAl_2O_4$(100), which specifically addresses the importance of the imaging distance and the atomistic nature of the tip termination. Based on detailed force-distance calculations, we show that it is even possible to discriminate between Al^{3+} and Mg^{2+} species in so-called antisite defects and cation vacancies located in the surface due to their different force interactions with a charged tip.

II. THE $MgAl_2O_4$(100) SURFACE

Bulk $MgAl_2O_4$ adopts the so-called normal spinel structure described by a slightly deformed cubic close packed lattice of oxygen atoms, with Mg^{2+} and Al^{3+} occupying the tetra-

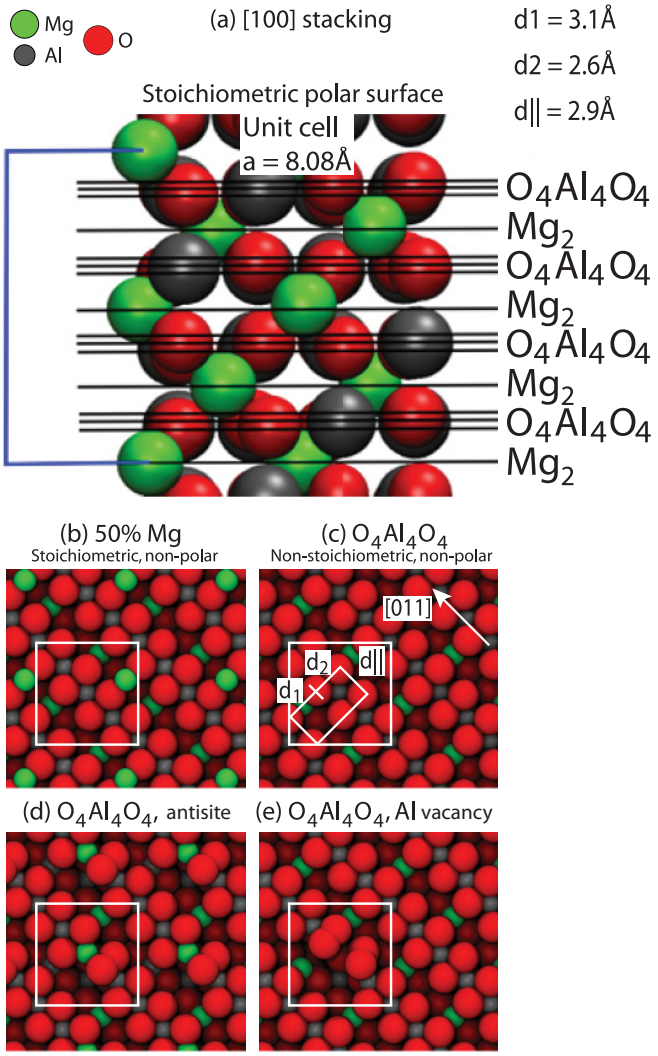

FIG. 1. (Color online) (a) Side view of a ball model showing the bulk structure of $MgAl_2O_4$ spinel. (b) The stoichiometric 50% Mg-terminated surface. (c) Nonstoichiometric surface terminated by an O_4-Al_4-O_4 layer formed by removing the Mg atoms from the bottom and top layers. (d) and (e) Same O_4-Al_4-O_4 surface termination as in (c), however, with a surface incorporated antisite (d) and an Al vacancy (e).

hedral and octahedral interstices respectively. As illustrated in Fig. 1(a), the stacking sequence in the [100] direction is Mg_2-O_4-Al_4-O_4, which yields in principle two different surface terminations obtained by cleaving the crystal above or below an Mg_2 layer, as illustrated in Figs. 1(b) and 1(c), respectively, creating an Mg or O_4-Al_4-O_4-terminated surface. Both (100) terminations expose so-called polar surfaces when cleaved stoichiometrically, and previous theoretical studies have calculated the surface energy of these different terminations[7,10–12,14,25] and also estimated the percentage of atoms that need to be removed in order to fulfill the polar stabilization criteria.[26] In a simple picture, the Mg_2 and $O_4Al_4O_4$ stacks can be regarded as a series of layers with alternating charge of equal magnitude analogous to a series of capacitors, each holding a certain charge density.[27] This arrangement causes the electrostatic potential to increase proportionally to the number of crystal layers and results in a surface instability when the diverging potential is added to the total surface energy. Ideally, the polarity can be cancelled by moving charge (half of the Mg atoms) to the top layer from underneath the crystal, as illustrated in Fig. 1(b). This new arrangement adopts a (2 × 2) unit cell that ensures that the macroscopic surface dipole is cancelled while maintaining a charge neutral crystal. The Mg-terminated (100) surface with only half the surface Mg sites occupied (Mg 50%) is considered,[7,11,14] ignoring the effect of adsorption from the ambient, to be the overall most stable surface termination that complies with the polar stabilization requirements. However, a nonstoichiometric O_4-Al_4-O_4 surface, which may be stable under certain conditions, can be created by removing the remaining Mg atoms from both the top and bottom crystal layers, as illustrated in Fig. 1(c). Here, the charged layers are also arranged such that the electrostatic potential is not diverging. However, since charges are removed, another nonideal situation arises because the crystal is no longer charge neutral. Naturally, this has to be compensated, and the possible stabilization mechanisms can be attributed to various phenomena in the surface layer, like charge transfer, adsorption of foreign species, reconstruction, etc.[28] Due to the excess O contained on the O_4-Al_4-O_4-terminated surface, the stability will also depend on the conditions under which the surface is exposed. In Ref. 7, DFT calculations, coupled with a thermodynamic model that takes into account the chemical potential of adsorbing O species, showed that the introduction of O_2 gas changes the stability so that the O_4-Al_4-O_4-terminated surface is most stable in an oxygen containing environment, except at very high temperatures. Specifically, for the conditions used in the experiment reported here, the O_4-Al_4-O_4-terminated surface [Fig. 1(c)] is more stable than the 50% Mg-terminated surface [Fig. 1(b)] in a 10^{-7} mbar O_2 and 10^{-10} mbar H_2 atmosphere below a temperature of 700 °C.

III. METHODS

A. Sample preparation

The experiments were performed in a standard ultra-high vacuum (UHV) system with a base pressure better than 1×10^{-10} mbar. The UHV system is equipped with scanning tunneling microscope(STM)/atomic force microscope(AFM), x-ray photoelectron spectroscopy (XPS) and means for high-temperature annealing of the sample. The $MgAl_2O_4$ crystal was purchased from MTI Corporation with an EPI polished (100) facet. To prepare the crystal for NC-AFM experiments, it was first rinsed in a 1:1 mixture of nitric acid (65%) and water followed by annealing in a furnace at 1000 °C for 4 hours. The $MgAl_2O_4$ crystal was then mounted in a Ta sample holder (modified Omicron DC-sampleholder) with a thin tungsten foil clamped on the backside. After introduction of the sample to UHV, the sample could then be annealed by sending an electric current of 5–7 A through the tungsten foil, allowing for sample temperatures of up to approximately 1250 °C. To clean the sample, it underwent cycles of Ar^+ sputtering (10 minutes at 1 keV) followed by annealing (15 minutes at 1100 °C and a 2 °C/s temperature ramp) and cooling down to approximately 100 °C in an oxygen atmosphere (1×10^{-7} mbar). The sample temperature was monitored contact

free on the face of the crystal using an optical pyrometer (Metis MY81, Sensortherm GmbH), which was precalibrated against measurements with a K-type thermocouple in direct contact with the sample. After approximately 10 such cleaning cycles, the crystal was sufficiently flat and clean for performing NC-AFM. We monitored the surface cleanliness by x-ray photoelectron spectroscopy (XPS) using Mg K_α radiation (Phoibos 100 analyzer and XR 50 source, SPECS GmbH, Berlin, Germany). X-ray photoelectron spectroscopy spectra were recorded with the surface normal pointing in the direction of the analyzer and revealed the presence of only Mg, Al, and O. X-ray photoelectron spectroscopy spectra were recorded regularly during the preparation, and the stoichiometry of the crystal was not observed to change as function of the number of preparation cycles.

B. Noncontact atomic force microscopy

The NC-AFM images were all recorded at room temperature with a modified Omicron VT-AFM/STM contained in the UHV chamber. To improve imaging results, FM demodulation and cantilever oscillation control were performed with easyPLL-plus electronics from Nanosurf GmbH. Silicon cantilevers (PPP-NCH) from Nanosensors (Neuchatel, Switzerland) with a resonance frequency of $f_0 \approx 330$ kHz and a force constant of 42 N/m were utilized. Before usage, the tips were sputtered for a very short duration (5–10 s) at low energy, which is enough to remove the native SiO_2 layer without significantly blunting the tip. The NC-AFM measurements were performed by oscillating the cantilever at its first resonance with constant amplitude and monitoring the frequency shift (Δf) while raster scanning the tip across the surface, in either constant Δf or constant height (Z) mode. To achieve the highest possible resolution, all the atomically resolved NC-AFM images presented in this paper were recorded in the constant height mode, which has proved to be very reliable for imaging on the atomic scale.[29] The recorded signal constituting the atomic resolved images is thus the detuning (Δf), and the image contrast is directly comparable with the NC-AFM simulations, as described in the next section. Finally, a bias is applied to the surface with respect to the tip (U_{bias}), which is monitored and adjusted regularly in order to minimize the electrostatic forces arising from the contact potential difference (CPD).

The frequency set point, at which the optimal atomic resolution could be obtained, varied somewhat from experiment to experiment in the data considered here, reflecting the fact that the macroscopic sharpness (tip apex radius) of the AFM tip and therefore the long-ranged van der Waals (vdW) forces varied from tip to tip and from experiment to experiment.[29] When comparing experimental NC-AFM images with theoretically calculated images, the variations in the tip sharpness, as evident from the wide range of detuning set points, are however not a problem, since the long-ranged vdW forces can be accounted for rather precisely in the theoretical modeling. We found that the variation of the vdW contribution due to the macroscopic tip shape did not change the qualitative appearance of the resulting force curves. We therefore restrict our discussion to a semiquantitative discussion of the contrast arising from variations in the structure of the AFM nanoapex, but the variations in the contrast described in this paper should be valid for both sharp (low absolute Δf) and more blunt tips (high absolute Δf). An exact quantitative correspondence of the image corrugation may be obtained for images obtained with a specific tip by fitting the vdW contribution, as was done in Ref. 30.

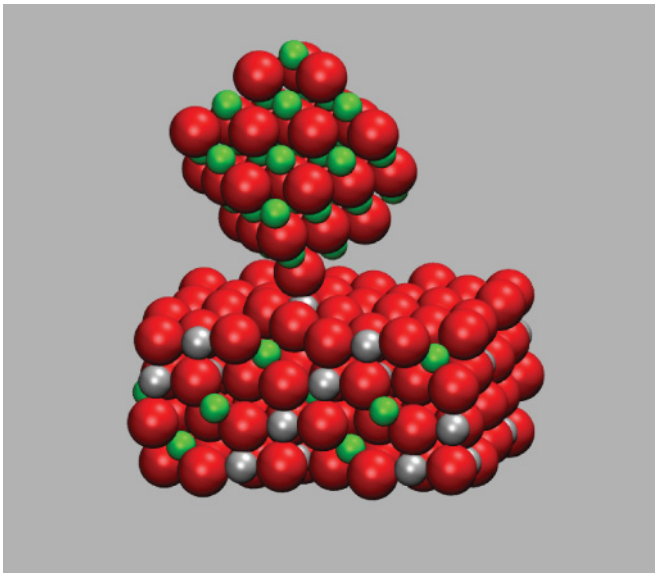

FIG. 2. (Color online) Tip-surface unit cell used in simulations. The upper part reflects the tip apex model as an MgO cube, which in this situation is oriented to expose an O-terminated tip. The lower part shows the O_4-Al_4-O_4 surface of $MgAl_2O_4$(100).

C. NC-AFM simulations

The calculations of the tip-surface interaction for NC-AFM simulations have been performed using the periodic plane-wave basis VASP code,[31,32] implementing the spin-polarized density functional theory (DFT) and the generalized gradient approximation. Projected augmented wave (PAW) potentials[33,34] were used to describe the core electrons. The potential for O was generated in the electron configuration $[1s^2]2s^22p^4$, Mg in $[Ne]3s^2$ and Al in $[Ne]3s^23p^1$, with the core electrons given in square brackets. A kinetic energy cutoff of 450 eV was found to converge the total energy of the tip-surface systems to within 10 meV. Systematic k-point convergence was checked for smaller bulk and surface calculations, but for the large surface unit cell used in the NC-AFM simulations, the gamma point was sufficient. The properties of the bulk and surface of $MgAl_2O_4$ were carefully checked within this methodology, and excellent agreement was achieved with experiments. A surface unit cell of $2 \times 2 \times 2$ was used (see Fig. 2) with a large vacuum gap, so that there was no artificial interaction between the tip and periodic images of the surface. The bottom layer of the surface was frozen to represent the bulk, while atoms in the upper layers were free to relax.

It is well known that NC-AFM tips, despite being originally silicon, are contaminated by the ambient and contact with the surface, hence their structure and chemistry is unknown on the nanoscale at the tip apex. In order to represent this, we consider that the tip has been contaminated by surface oxide

material. The tip used for the simulations was a $Mg_{32}O_{32}$ cube, which, depending on its orientation in relation to the surface, was functionalized with an Mg or O atom pointing towards the surface (see Fig. 2), to mimic a positively or negatively polarized tip apex, respectively.[35] The forces experienced by the model tips are explicitly calculated for heights of 0.2 to 0.5 nm above the surfaces, with a sampling of 0.05 nm. The lower third of the tip atoms were free to relax, while the remaining atoms were frozen to represent the interface to the macroscopic tip. Depending on the symmetry of the surface 13–21 force-vs-distance curves are calculated over the surface with each tip for a total of 208–336 calculations per system. Careful interpolation is used to provide a finer mesh for simulating images. In order to compare directly to experimental frequency changes, the calculated tip-surface forces are used as input for a model of cantilever dynamics using experimental parameters.[35] The simulated images are fitted to the experimental images by adjusting the imaging distance (Z) to the value yielding the best resemblance. The optimum Z values found are 0.30 and 0.25 nm for the O and the Al lattice, respectively. The distances are different for the two imaging modes, but this is consistent with the fact that the two modes are not observed in the same image experimentally, as was previously observed for TiO_2(110).[36]

As in previous modeling studies,[29,37–40] tip-induced displacements of atoms in the surface and corresponding displacements of atoms in the tip play an important role in contrast formation. While detailing all possible displacements of every surface site at each height and for each tip-system combination would be overwhelming, here we will discuss some of the key processes.

For the negative terminated tip, the main displacements are observed when the tip is over the cations in the surface. On the ideal surface, as the tip approaches Al sites, the Al atoms displace towards the tip, reaching a maximum displacement of 0.1 nm at a tip-surface distance of 0.3 nm before being pushed back into the surface. The oxygen at the tip apex displaces towards the surface during approach, up to a maximum of 0.03 nm at 0.3 nm distance. Approach over the subsurface Mg sites in the ideal surface showed no strong displacements. On the inversion defected surface, when approaching the surface Mg site, strong displacements of the Mg are also seen, up to 0.1 nm towards the tip at a height of 0.3 nm. This displacement also induces movement of the oxygen atoms surrounding the Mg upwards by about 0.03–0.05 nm.

Equivalently, for the positively terminated tip, the strongest displacements are observed when over oxygen atoms in the surface, particularly those with lower coordination due to defects. For the ideal surface and the inversion-defected surface, there is displacement of surface oxygen by about 0.08 nm at a tip height of 0.3 nm, and then they are pushed back into the surface. At oxygen next to the inversion defect, this increases to 0.11 nm due to their lower bonding coordination. Tip displacements are always also present, with the apex ion displacing towards the surface by about 0.02 nm at a height of 0.3 nm, and then moving into the tip as the surface atom is pushed back into the surface.

Calculations of the vacancy site demonstrate a similar pattern to the other surfaces, but the severely undercoordinated oxygen around the vacancy dominates the displacements. For example, when a negative terminated tip approaches very close (0.2 nm or less) to the Al atoms, either side of the vacancy, the neighboring oxygen pair actually jumps out of the vacancy site and bonds to another site to avoid the repulsive negative-negative ion interaction. When approaching the oxygen pair with a positively terminated tip, it actually reorients so that one oxygen atom displaces by 0.1 nm at a tip height of only 0.4 nm—the O-O molecule is almost vertical, before returning to an in-plane configuration as it is pushed in by the tip.

We checked our simulated results on the ideal surface, inversion-defected surface, and vacancy surface for large jumps in forces that could indicate likely instabilities. Of the force curves that demonstrated this behavior, only a few cases seemed to show instabilities when analyzing the atomic structures, i.e. a large displacement at a single tip height, rather than the development of a large displacement over several tip heights. In particular, when imaging the ideal or inversion-defected surface with a negative terminated tip, there was a large jump of the Al atom towards the tip at an imaging distance of about 0.3 nm, with the Al displacing upwards by around 0.1 nm. Tip displacements towards the surface were smaller, of the order of 0.02 nm. Also, again at a height of 0.3 nm when imaging the defected surface with a positive tip, there is a large displacement of oxygen (over 0.1 nm) directly around the inversion defect. For the Al vacancy, the only instability observed was actually in the position of the paired oxygen atoms near the vacancy. While this is not really instability, since it never jumps to the tip, there are significant displacements when the negative tip comes very close to the surface and the positive ions in the second layer of the tip are close to the oxygen pair. It should be noted that even these could be partially exaggerated by the sampling of the theoretical points along the z direction (0.05 nm), but a finer grid directly scales the computational effort while not affecting the general conclusions.

IV. NC-AFM CONTRAST FORMATION ON THE CLEAN $MgAl_2O_4$ (100) SURFACE

Figures 3(a) and 3(b) show experimental atom-resolved NC-AFM images of the clean O_4-Al_4-O_4-terminated surface of $MgAl_2O_4$(100), which is the starting point of the discussion in this paper. The two NC-AFM images in Figs. 3(a) and 3(b) reflect complementary NC-AFM imaging modes where the contrast is different due to the presence of differently terminated AFM tips during the experiments. Images representative for both modes were observed during the same experiment, and the switch in contrast is therefore attributed to changes in the tip apex that occur during scanning, e.g. by contact with the surface.[17,41] Previous studies have shown elegantly how differently terminated AFM tips may be used to identify and discriminate between the separate sublattices of some ionic compounds, such as KBr,[42] NaCl,[43] and CaF_2.[44] Specifically, for the case of TiO_2(110), NC-AFM experiments and DFT-based simulations showed that the NC-AFM image contrast in this case depends strongly on the charge state of the tip apex. Based on the detailed model of the tip apex obtained in each case, it was then possible to chemically identify surface defects on TiO_2(110) as either O-vacancies or OH groups.[30]

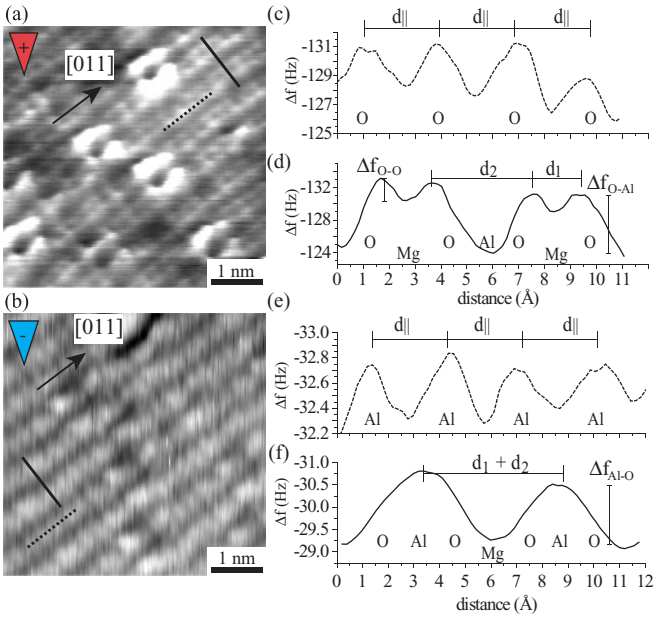

FIG. 3. (Color online) Experimental NC-AFM images of the (a) oxygen and (b) aluminum lattice obtained with a positive and a negative tip apex, respectively. Line scans (c) and (d) illustrate the periodicities measured on the oxygen lattice (a) with a positive tip. Line scans (e) and (f) illustrate the periodicities measured on the Al lattice (b) with a negative tip. In both lattices, the distances $d_{\|}$ and $d_1 + d_2$ match the values from the structural model in Fig. 1(c). NC-AFM parameters: (a) $df_{\text{set}} = -126$ Hz, $A_{p\text{-}p} = 10$ nm, $U_{\text{bias}} = 1.0$ V (b) $df_{\text{set}} = -30$ Hz, $A_{p\text{-}p} = 10$ nm, $U_{\text{bias}} = 3.0$ V.

In this paper, we successfully extend this methodology to the case of the complex ternary $MgAl_2O_4(100)$ surface.

As illustrated in the top-view ball model in Fig. 1(c), the most stable O_4-Al_4-O_4-terminated surface of $MgAl_2O_4(100)$ exposes a structure which is defined by a sublattice of Al atoms (grey), which are arranged in rows with an interatomic distance of $d_{\|} = 2.9$ Å along the rows and with a distance of 5.7 Å ($d_1 + d_2$) between the rows, and a sublattice of O atoms (red/dark grey), which are arranged in double rows spaced ($d_1 + d_2$) = 5.7 Å apart and with a $d_{\|} = 2.9$ Å periodicity along the rows. This oxygen double-row feature occurs because the oxygen rows are spaced apart with alternating distances $d_1 = 3.1$ Å and $d_2 = 2.6$ Å. Mg atoms (green/light grey) are located in the subsurface region arranged in a quadratic lattice with a 5.7 Å spacing. Thus, following an interpretation scheme where the NC-AFM contrast is dominated by electrostatic interactions, Fig. 3(a) can be accounted for as an atomically resolved image obtained with a positive tip, where the double rows of O atoms which terminate the O_4-Al_4-O_4 surface are clearly resolved, and Fig. 3(b) can be attributed to an NC-AFM image recorded in the complementary imaging mode reflecting a negatively charged tip apex in which the position of the surface cations is resolved with a bright contrast. In Figs. 3(c) and 3(e) are shown frequency shift line scans along the oxygen and aluminum rows for the positive and negative tip termination, respectively, which both reflect the periodicity of $d_{\|} = 2.9$ Å. This corresponds exactly to the distance between Al or O atoms, respectively along the rows (in the [011] direction) on the bulk-truncated O_4-Al_4-O_4-terminated surface. Figures 3(d) and 3(f) show line scans perpendicular to the oxygen and aluminum rows for the positive and negative tip termination, respectively, and again illustrate the match with the structural model of an unreconstructed O_4-Al_4-O_4-terminated surface with a periodicity of $d_1 + d_2 = 5.7$ Å between rows.

Consequently, the images in Figs. 3(a) and 3(b) can qualitatively be interpreted by direct comparison with the symmetry and geometrical position of the oxygen atoms and cations, respectively, on the O_4-Al_4-O_4-terminated surface. In the following sections, we investigate by means of such experimental and DFT-based simulated images to which extent both the qualitative and quantitative contrast depends on the tip-surface distance, for the positive and a negative tip apex, respectively.

A. O_4-Al_4-O_4-terminated $MgAl_2O_4(100)$: Positive tip imaging mode

Figure 4(a) illustrates a series of representative NC-AFM simulations which demonstrate the expected qualitative Z dependence of the image contrast on the O_4-Al_4-O_4-terminated surface for a positive tip when the tip-surface distance is increased in steps from 2.5 to 4.0 Å. The superimposed ball models illustrate the position of O and Al in the topmost layer, and Mg in the subsurface layer. As expected, the bright contrast is always located on the double-O rows, whereas the aluminum rows are always imaged with the darkest contrast. This is shown in further detail in the calculated Δf-vs-distance curves for the complete Z range in Fig. 4(b) for the most representative O, Mg, and Al sites on the O_4-Al_4-O_4-terminated surface (spectroscopy sites are indicated on the simulated image at $Z = 2.5$ Å). The larger the negative detuning (Δf), the higher the contrast in the AFM image (note the inverted frequency scale). Here, the Al sites always have a lower absolute Δf value, and the difference between O and Al sites always reflects a higher contrast on the O rows. A close inspection of the simulations in Fig 4(a), however, reveals that two different contrast regimes can be defined: when imaging close to the surface ($Z = 2.5$–3.0 Å), all oxygen atoms in the surface are clearly resolved, and the double oxygen rows are clearly revealed [see line scan in Fig. 3(c) at $Z = 3.0$ Å]. When increasing the tip surface distance ($Z = 3.5$–4.0 Å), the resolution of the distance d_1 is lost ($\Delta f_{\text{O–O}}$ approaches zero) between the pairs of O in a double row, as illustrated with a line scan at $Z = 4.0$ Å in Fig. 4(c). The oxygen atoms are then resolved pairwise, and instead, a very weak double periodicity in the direction of the O row is giving rise to a quadratic unit cell (marked with a black square). This feature reflects the underlying quadratic Mg lattice, i.e. the oxygen atoms bound to Mg are slightly more susceptible to tip-induced displacements due to the weaker binding (the other oxygen pair lies directly above a subsurface Al), and this results in an increase in contrast at larger tip-surface separations. However, from the line scan in Fig. 4(d), at $Z = 4.0$ Å, it is evident that the corrugation of this feature is in fact very small, approximately 0.1 Hz, which is lower than the typical noise level of our NC-AFM setup (~0.5 Hz). At even larger distances ($Z \geqslant 4.0$ Å), the corrugation of this double periodicity along the oxygen rows gets even smaller, resulting in the oxygen double rows being imaged as single bright rows with an inter-row distance of

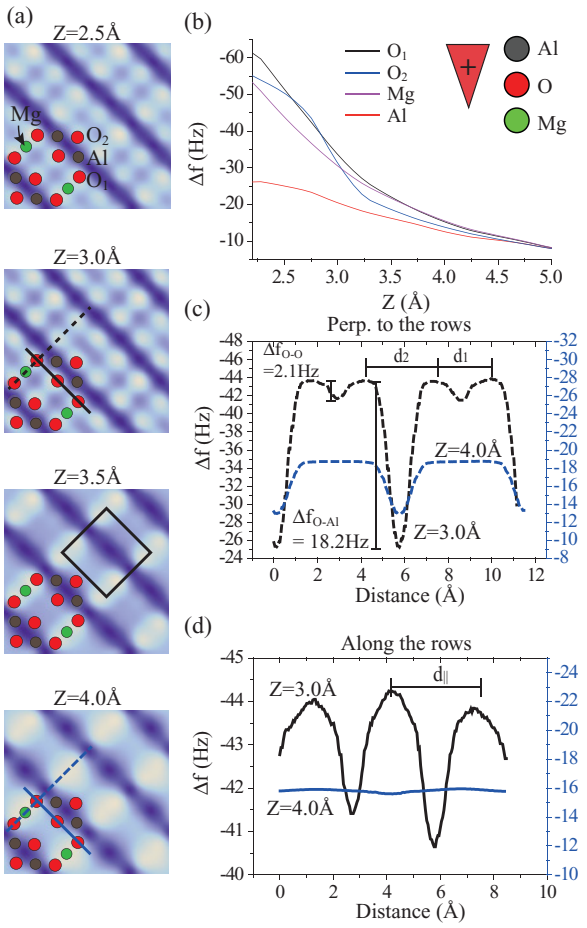

FIG. 4. (Color online) (a) NC-AFM simulations of the O_4-Al_4-O_4-terminated surface utilizing a positively charged tip apex. Images are shown as the tip-surface distance Z is varied from 2.5 to 4.0 Å. (b) Spectroscopy curves showing the detuning as a function of tip-surface distance at four different surface sites. (c) Line scan perpendicular to the oxygen rows (marked in the images with dashed lines) at $Z = 3.0$ Å shows how the distance between two oxygen atoms (d_1) is clearly resolved; however, at $Z = 4.0$ Å, this distance is no longer well defined. (d) Line scans along the rows (marked with solid lines) show how the corrugation of the oxygen atoms decreases when going from $Z = 3.0$ to 4.0 Å. At $Z = 4.0$ Å, the periodicity doubles ($2 \times d_{\|}$, quadratic unit cell indicated in $Z = 3.5$ Å image), however, the corrugation is 0.1 Hz, which is approximately the resolution limit in our NC-AFM setup.

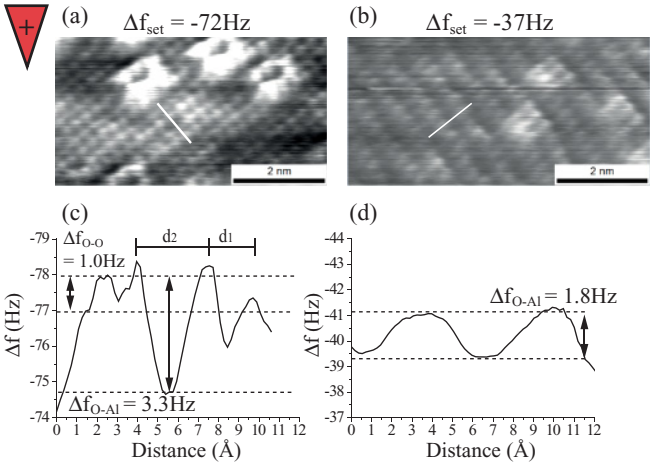

FIG. 5. (Color online) Experimental NC-AFM images recorded within a short time period with the same positively charged tip. (a) Image recorded with $df_{\text{set}} = -72$ Hz showing the oxygen atoms fully resolved close to the surface. (b) Far from the surface at $df_{\text{set}} = -32$ Hz, the oxygen atoms are resolved in pairs. (c) Line scan belonging to the image in (a) illustrating the corrugation of the double-row oxygen atoms. (d) Line scan belonging to the image in (b) illustrating how the corrugation $\Delta f_{\text{o-o}}$ equals zero when scanning at larger Z, thereby resolving the oxygen atoms in pairs. NC-AFM parameters for both images: $A_{p\text{-}p} = 10$ nm, $U_{\text{bias}} = 2.1$ V

5.7 Å, corresponding to $d_1 + d_2$ in Fig. 1(c). Our experimental series of NC-AFM images recorded at different tip-surface distances are in good agreement with this Z dependence predicted from the simulations. Figures 5(a) and 5(b) illustrate two images, extracted from a series of images recorded with the same stable tip termination. In order to adjust the imaging distance Z, df_{set} was increased in steps from -72 Hz [see Fig. 5(a)]. Note that, the atomic rows in Fig. 5(a) are rotated by 90° with respect to the rows in Fig. 5(b), which can be explained by the fact that the two images are recorded on adjacent terraces separated by $a/4 = 2.02$ Å. The two experimental images in the figure also reflect the observation that, when imaging close to the surface ($df_{\text{set}} = -72$ Hz), all the oxygen atoms in the double rows are clearly resolved, and the experimental image clearly matches the simulations in the distance range 2.5–3.0 Å in Fig. 4(a). As illustrated in the line scan in Fig. 5(c), the height corrugation of the O atoms relative to the Al atoms ($\Delta f_{\text{O-Al}}$) is measured to be 3.3 Hz, whereas the height corrugation resolving the O pair ($\Delta f_{\text{O-O}}$) is approximately 1.0 Hz. When the imaging distance is increased, $\Delta f_{\text{O-Al}}$ decreases monotonously, and at the experimental value ($df_{\text{set}} = -37$ Hz), $\Delta f_{\text{O-Al}}$ has decreased to a value of 1.8 Hz on average [Fig. 5(b) and 5(d)]. Furthermore, at this distance, the oxygen atoms are not distinguishable anymore, corresponding to a vanishing $\Delta f_{\text{O-O}}$. This situation is equivalent to the simulation in Fig. 4(a), at $Z \geqslant 3.5$ Å. Increasing df_{set} further from here decreases the corrugation of the oxygen atoms even more, and finally, at $df_{\text{set}} = -32$ Hz (image not shown here), the tip-surface interaction becomes so weak that also the $\Delta f_{\text{O-Al}}$ corrugation approaches zero.

As stated in the previous section, the distances d_1 and d_2 measured from peak to peak in the experimental images [see line scan in Fig. 5(c)] are not directly comparable with the structural model of the O_4-Al_4-O_4-terminated surface [see Fig. 1(c)]. That is, in the experimental images, the distance d_1 is measured to be smaller than d_2, although the oxygen atoms are actually geometrically arranged in an opposite way such that d_2 is smaller than d_1 [see ball model in Fig. 1(c)]. However, this exact behavior is perfectly reproduced in the NC-AFM simulations, as shown with the line scan in Fig. 4(c), and illustrates how the NC-AFM contrast in this case is not a direct topographic reflection of the surface. The line scan from the simulated image clearly shows that d_1 is smaller than d_2, precisely as observed in the experimental images. Due to the domination of the electrostatic forces, the tip experiences an asymmetry when scanning over an oxygen atom because the

Al^{3+} screens the negative charge more efficiently compared to the Mg^{2+} located deeper in the surface. Therefore, the relatively high positive charge of the Al^{3+} cation tends to shift away the contrast peak originating from the oxygen atoms [see line scan Fig. 3(d)], which then makes d_2 appear larger than the actual geometrical distance. Simulations thus confirm that the measured NC-AFM contrast fits the structural model of the oxygen lattice and that the dark rows can indeed be ascribed to the Al rows on the O_4-Al_4-O_4-terminated surface. The simulations [see line scan in Fig. 4(c)] estimate the row distances to be $d_1 = 2.3$ Å and $d_2 = 3.4$ Å, whereas the same distances are measured to be $d_1 = 2.0 \pm 0.1$ Å and $d_2 = 3.7 \pm 0.1$ Å in experiments [Fig. 3(d) and Fig. 5(c)], which suggests that this screening effect of the oxygen atoms is slightly underestimated in the simulations.

B. O_4-Al_4-O_4-terminated $MgAl_2O_4$(100): Negative tip imaging mode

The Z variation of the negative tip imaging mode can be accounted for using the same methods as above. Figure 6(a) illustrates a series of representative NC-AFM simulations of the O_4-Al_4-O_4-terminated surface for a negative tip when the tip-surface distance Z is increased in steps from 2.5 to 4.0 Å. As expected from the polarity of this tip, the contrast is now inverted, and the Al sublattice is always imaged with a bright contrast, whereas the oxygen rows are reflected by the regions with the darkest contrast. The Δf-vs-distance curves above the O, Mg, and Al sites on the O_4-Al_4-O_4-terminated surface for the complete Z range utilizing the negative tip in Fig. 6(b) again show a monotonous behavior with no crossover regions. The difference between O and Al sites always reflects a higher contrast on the Al rows, which increases upon decreasing the Z distance. The simulations in Fig. 6(a) also show an overall variation when varying Z: at close imaging distances ($Z = 2.5$–3.0 Å), the aluminum atoms are all clearly resolved, appearing as bright protrusions along the rows with an inter-row spacing corresponding to $d_1 + d_2$. At larger distances ($Z = 3.5$–4.0 Å), the direct regularity of the Al sublattice ($d_\parallel$) is broken, and the surface unit cell becomes vaguely quadratic (marked with a black square), and the corrugation decreases dramatically. This is illustrated in Fig. 6(d), where at $Z = 3.0$ Å, the periodicity along the aluminum rows, $d_\parallel$, is clearly resolved. However, at $Z = 4.0$ Å, the corrugation along the aluminum rows has decreased to approximately 0.03 Hz, which is much below the experimental noise, and therefore the distance $d_\parallel$ should not be resolved in NC-AFM experiments. As illustrated in Fig. 6(c), the corrugation measured across the aluminum rows, $\Delta f_{\text{Al-O}}$, decreases to 0.3 Hz at $Z = 4.0$ Å, which means that the aluminum rows are resolved even though every single Al along the rows is not. The appearance of a quadratic lattice reflects an onset of a force contribution emanating from the Mg lattice in the subsurface layers, as for the Mg-terminated tip. This is due to a generally slower decay of these forces compared to outward relaxation effects of the Al atoms, which dominate for the O-terminated tip at short distances. It should be noted that the quadratic unit cell, observed in the simulations, for distances $Z \geqslant 3.5$ Å [marked by the black square in Fig. 6(a)] has contrast peaks that are not in registry with the

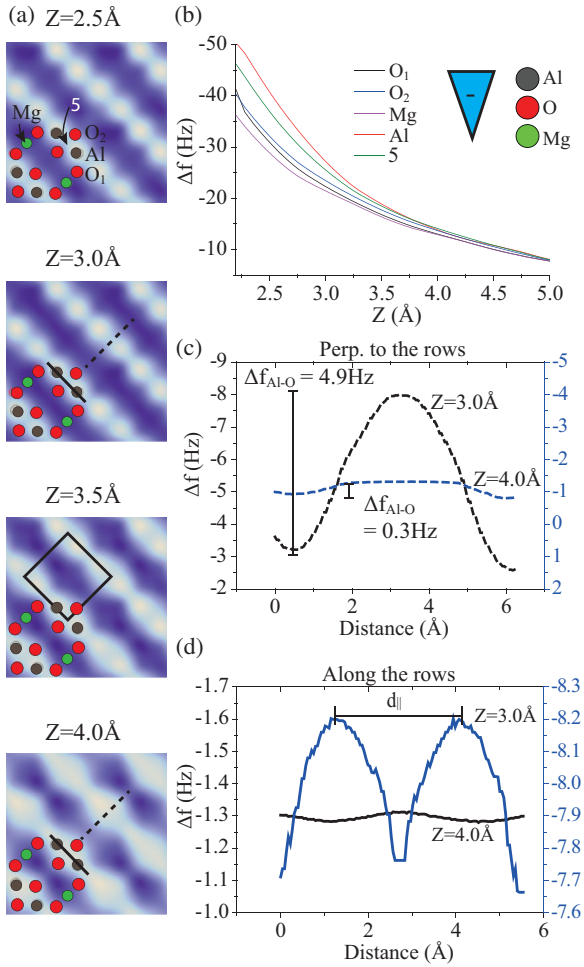

FIG. 6. (Color online) (a) NC-AFM simulations of the O_4-Al_4-O_4-terminated surface utilizing a negatively charged tip apex. Images are shown as the tip-surface distance Z is varied from 2.5 to 4.0 Å. (b) Spectroscopy curves showing the detuning as a function of tip-surface distance at four different surface sites. (c) Line scans perpendicular to the Al rows (marked by dashed lines in the images) illustrating how the corrugation decreases as the tip-surface distance is increased from $Z = 3.0$ to 4.0 Å. (d) Line scans along the Al rows (marked by solid lines in the images) illustrating how the corrugation of the Al atoms along the rows decreases when scanning at large tip-surface distance. At $Z = 3.5$ Å, a double periodicity starts to arise (marked by black square).

Al lattice. This is seen clearly from the line scan in Fig. 6(d) at $Z = 4.0$ Å, where the contrast maximum is placed in between two Al sites. The Al sites are not really resolved individually at all, and the periodicity comes from the reduction of contrast near the Mg sublattice.

The trends from the simulation are also observed for the experimental images recorded with a negatively charged tip apex. Two images extracted from a larger series of experimental images, recorded at different tip-surface distances, are shown in Figs. 7(a) and 7(b). Both images are recorded with the same tip within a short time period, and no tip changes were observed during scanning. In the image recorded with a $df_{\text{set}} = -48$ Hz (smallest Z), the aluminum atoms are all clearly resolved along the rows, and the average corrugation between the Al sites and the dark O-row ($\Delta f_{\text{Al-O}}$) is determined from the line scan in

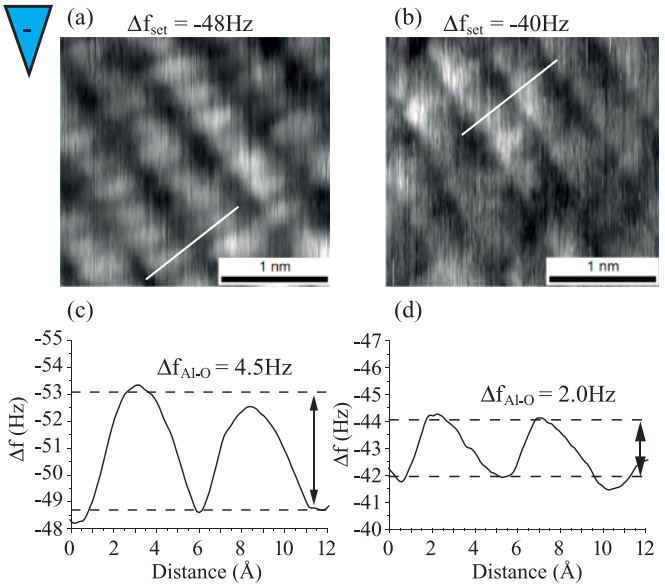

FIG. 7. (Color online) Experimental NC-AFM images recorded within a short time period with the same negatively charged tip. (a) Close to the surface ($df_{set} = -48$ Hz), the aluminum atoms are fully resolved. (b) Far from the surface ($df_{set} = -40$ Hz), the rows are still resolved; however, the aluminum atoms along the rows are no longer resolved. (c) Line scan illustrating the corrugation of the Al rows in image (a). (d) Line scan showing how the corrugation decreases when scanning at larger tip-surface separation in image (b).

Fig. 7(c) to be 4.5 Hz. When df_{set} is slightly increased, the aluminum atoms are still reasonably well resolved; however, the $\Delta f_{Al\text{-}O}$ corrugation is decreasing monotonously as also observed in the simulated images in Fig. 6(a) when increasing Z. In the image in Fig. 7(b), the df_{set} is increased to -40 Hz. In this case, the image became fuzzy, and the corrugation of the aluminum rows is lowered to approximately 2.0 Hz. At this distance, the aluminum atoms are now very poorly resolved along the rows, and the image now consists of bright rows, reflecting the predicted qualitative contrast in Fig. 6(a), where only the rows are resolved at large Z and not the Al atoms along the rows. The quadratic surface unit cell predicted by simulations was not observed in the experimental images. This can be explained by the fact that the quadratic unit cell is only present in a narrow Z range. Furthermore, as also mentioned above, the detuning corrugation affiliated with this quadratic feature is very small and probably not possible to detect.

C. 50% Mg-terminated $MgAl_2O_4(100)$: NC-AFM image simulations

As previously mentioned, a Mg-terminated surface in which half of the Mg atoms are removed to fulfill the stabilization criteria may arise from sample preparation at very reducing, high-temperature conditions and may also result from cleaving $MgAl_2O_4(100)$ samples. This surface termination was not observed in our experiments,[7] but we present here the simulated NC-AFM images for future reference. The simulated images show in an unambiguous way that the 50% Mg-terminated surface is not consistent with the experimental NC-AFM images. The (2×2) 50% Mg-terminated $MgAl_2O_4(100)$ surface adopts the structure illustrated in Fig 1(b) and is described by a 8.08 $\times$ 8.08 Å^2 quadratic unit cell (same length as the spinel unit cell) superimposed on the O_4-Al_4-O_4 surface.

Figures 8(a) and 8(b) show a simulated series of NC-AFM images of the 50% Mg-terminated $MgAl_2O_4(100)$ surface recorded with a positively and a negatively terminated tip, respectively. The ball models on top of the simulated images indicate the positions of the atoms in the top three layers (Mg_2-$O_4Al_4O_4$-Mg). The spinel unit cell is marked by a black square indicating the lattice parameter of 8.08 Å. The contrast is strongly dependent on the imaging distance Z, as illustrated by the four simulated images shown for each tip mode ranging from $Z = 2.5$ to 4.0 Å. In the positive tip mode [Fig. 8(a)] at $Z = 2.5$ Å, the top-layer Mg atoms are not contributing significantly to the contrast, which is instead completely dominated by the underlying oxygen lattice. However, at a larger tip-surface separation [Z = 3.5 Å, Fig. 8(a)] the Mg atoms in the surface start to dominate the contrast and are now imaged as holes in the oxygen lattice. In the case of an Mg-terminated surface imaged with a positive tip, a distinct (2×2) quadratic lattice of holes on the O rows with side lengths of the unit cell (marked with a black square in all images) then characterizes this surface. A (2×2) structure was never observed in our experimental images. The simulated images of the Mg-terminated surface recorded with a negatively charged tip apex are illustrated in Fig. 8(b). At close distance [Fig. 8(b), Z = 2.5 Å], the contrast closely reflects that expected for a negative tip interacting with the surface cations, i.e. mainly the aluminum atoms are resolved with a superimposed (2×2) grid reflecting the Mg atoms. As the imaging distance is increased, the contrast originating from the Al atoms decreases, and at an imaging distance of

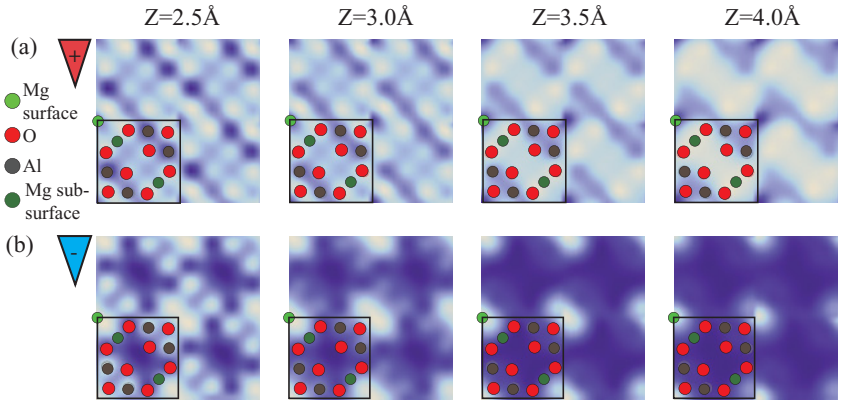

FIG. 8. (Color online) NC-AFM simulations of 50% Mg-terminated surface utilizing (a) a positively and (b) negatively charged tip apex. (a) Close to the surface, only the oxygen lattice is resolved; however, when increasing the tip-surface distance, Mg starts to appear as holes in the oxygen rows giving rise to a quadratic surface unit cell. (b) Close to the surface, both the Al and the Mg cations are resolved; however, with increasing tip-surface distance, only the Mg atoms are visible as protrusions giving rise to a quadratic surface unit cell.

$Z \geqslant 3.5$ Å [Fig. 8(b)], the contrast is solely influenced by the top-layer Mg atoms, which then constitute a quadratic lattice with side lengths of the unit cell, as marked by a black square on top the simulated.

Even for a sample annealed extensively at temperatures in excess of 1000 °C without oxygen gas, it was not possible to observe experimental NC-AFM images associated with the (2×2) 50% Mg-terminated surface in our studies. We attribute this to the fact that initial O treatment, needed to heal the crystal after sputtering, strongly stabilizes the O_4-Al_4-O_4 surface and that the conversion into the Mg-terminated surface requires the removal of Al in addition to O desorption, which is a process that may be strongly kinetically hindered. However, future NC-AFM studies on $MgAl_2O_4(100)$ samples cleaved in vacuum[45] may be able to access and resolve the structure of the 50% Mg-terminated $MgAl_2O_4(100)$ surface.

V. NC-AFM CONTRAST OF SURFACE DEFECTS ON $MgAl_2O_4(100)$

In the so-called normal spinel structure of $MgAl_2O_4(100)$, the divalent Mg^{2+} and trivalent Al^{3+} cations occupy tetrahedral and octahedral interstices in the O lattice, respectively [Fig. 1(a)]. However, the cation distribution may deviate from the ideal spinel arrangement in the bulk, and depending especially on preparation method and the heat treatment of the crystal,[8,46,47] some degree of inverse spinel disordering occurs. Inversion disordering is manifested by local interchange of an Al atom at octahedral sites with an Mg atom at neighboring tetrahedral interstitial sites, forming so-called antisite defects. The antisite disorder process can conveniently be described using the Kröger–Vink notation:[48] $Mg^X_{Mg} + Al^X_{Al} \rightarrow Mg'_{Al} + Al^{\bullet}_{Mg}$. Here Mg'_{Al} indicates an Mg^{2+} ion occupying an octahedral site which is normally occupied by an Al^{3+} ion, and vice versa for $Al^{\bullet}_{Mg}$. The superscript indicates the charge of the occupying species in relation to the normal charge at that site. The prime is used to denote a charge of minus one, whereas an asterisk and an X denote a positive and neutral charge, respectively. In addition to the antisites defects, isolated cation vacancies V''_{Mg} or V'''_{Al} may exist due to nonstoichiometric mixing of MgO and Al_2O_3 precursors during synthesis of spinel. Our recent NC-AFM studies[7] surprisingly showed that antisite formation is in fact energetically favored on both the O_4-Al_4-O_4-terminated surface and the 50% Mg-terminated surface of $MgAl_2O_4(100)$, and antisites associated with interchange of Mg and Al are therefore expected to be part of any surface termination of $MgAl_2O_4(100)$. This is in strong contrast to the antisite formation in the bulk, which is calculated to be endothermic with energy of 0.73 eV.[49] The ball model in Fig. 1(d) illustrates the most stable configuration for one antisite per unit cell on the O_4-Al_4-O_4-terminated surface from Ref. 7. The Mg from the subsurface position changes place with Al in the top layer, thus forming an Mg'_{Al} surface site and an $Al^{\bullet}_{Mg}$ site in the subsurface with a favorable energy of formation of -0.47 eV. At the same time, the O positions near the Mg'_{Al} site are slightly modified compared to the double-row structure on the clean surface. Here, V''_{Mg} or V'''_{Al} vacancies are generally very unfavorable in both bulk and surface $MgAl_2O_4$ with formation energies in the range

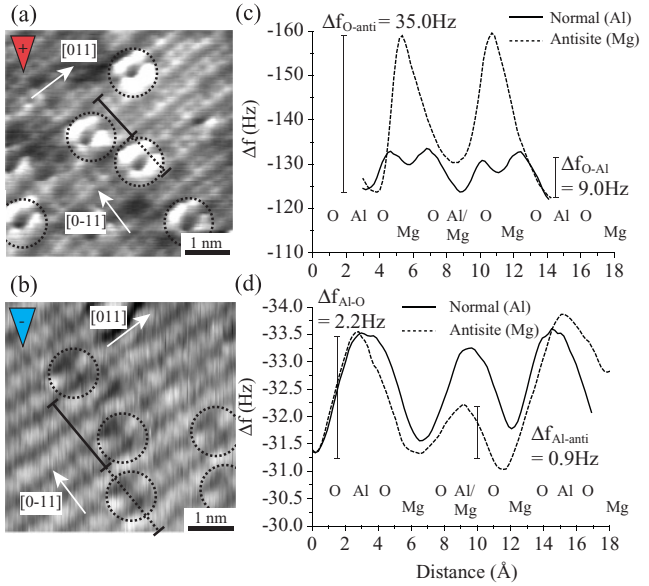

FIG. 9. (Color online) NC-AFM images of the (a) oxygen and (b) aluminum lattice. (c) Line scan across the oxygen rows [indicated by solid and dashed lines in (a)] illustrating the change in corrugation of the oxygen atoms when neighboring an antisite. (d) Line scan across the aluminum rows [indicated by solid and dashed lines in (b)] illustrating the decrease in contrast at antisites.

of 3–5 eV per vacancy.[7,49,50] The ball model in Fig. 1(e) illustrates the most favorable calculated structure for one V'''_{Al} per unit cell formed by removal of Al from the Al lattice on the O_4-Al_4-O_4-terminated surface, which, however, still has a formation energy of more than 3 eV, and such vacancies were therefore concluded not to be a predominant part of a well-annealed surface.[7]

The NC-AFM images in Figs. 9(a) and 9(b) reveal a number such antisite defects superimposed on the lattice defined by the O_4-Al_4-O_4-terminated surface for both the positive and the negative tip. The qualitative appearance of the defect in the NC-AFM image recorded with a positive tip [Fig. 9(a)] appears as a dark spot surrounded by a very bright region. Figure 9(c) illustrates a comparison of a line scan across the defect (dashed line) and the clean (solid line) surface, respectively, for an NC-AFM image recorded with a positive tip. As indicated by the atomic labels in Fig. 9(c), the center of the defect is located exactly on the Al lattice, i.e. on the rows with the darkest contrast on the clean surface. In the NC-AFM image for the negatively terminated tip in Fig 9(b), the defect is imaged as a depression occupying a single atomic site on rows defined by the Al atoms on the clean surface. The comparison of line scans again shows that the center of the defect is located directly on the Al lattice. The location, distribution, and symmetry in the area around the defects in the NC-AFM images are thus very consistent with the presence of thermodynamically favored antisite defects in the O_4-Al_4-O_4-terminated surface, which appear on the Al lattice as Mg is exchanged on the original Al sites (Mg'_{Al}) in Fig. 1(d).

As a first approach to understand the NC-AFM contrast formation at these defects, it is instructive to perform some qualitative considerations before analyzing the NC-AFM

simulations. Intuitively, NC-AFM imaging with charged tips appears as the ideal tool to study defect formation in ionic materials,[36,51,52] since charged tips are highly sensitive to even very small variations in the charge distribution in the surface. The cation inversion process on the Al sites, which is summarized as $Al^{X}_{Al} \rightarrow Mg'_{Al}$, effectively redistributes the charges associated with Mg^{2+} and Al^{3+}, so that Mg'_{Al} exposed to the surface has a 1-unit charge lower than the surrounding Al. Therefore, with a negative tip, the expected result is a lower attractive interaction on top of a Mg'_{Al} site, which is consistent with the NC-AFM observation in Fig. 9(b). For imaging with a positive tip, bright contrast is dominated by the oxygen atoms, which are not replaced, but the oxygen atoms around a Mg'_{Al} defect have a modified bonding due to the lower charge at the Al lattice site, which is also fully consistent with the NC-AFM image in Fig. 9(a). In principle, similar considerations apply to Al vacancy formation $Al^{X}_{Al} \rightarrow V'''_{Al}$, since, in this case, the Al^{3+} is replaced by a nominally neutral vacancy V'''_{Al}. However, the NC-AFM signature associated with the V'''_{Al} is expected to be much stronger than for antisites, due to the rather significant change of nominally 3-unit charges. In the intuitive picture based on qualitative consideration of the NC-AFM contrast, it is therefore *a priori* impossible to tell the difference between Mg'_{Al} and V'''_{Al} defects, and although thermodynamics rule out the vacancies, NC-AFM simulations are necessary to be able to differentiate between the two kinds of defects alone from NC-AFM experiments.

A. Antisites on $MgAl_2O_4$(100): Positive tip imaging mode

The line scans in Fig. 9(c) show a comparison of the experimental corrugation across two oxygen double rows with (dashed line) and without (solid line) the antisite defect in between. A pronounced feature of the defect site is that the two oxygen rows on both sides of the antisites located on the Al lattice are seen to exhibit a large increase in contrast compared to the oxygen rows with no neighboring antisite. As also illustrated by these line scans, the detuning corrugation increases from approximately 9.0 Hz ($\Delta f_{\text{O-Al}}$) for oxygen atoms far away from an antisite to 35.0 Hz ($\Delta f_{\text{O-anti}}$) for oxygen atoms neighboring an antisite. The strong contrast increase of the oxygen atoms surrounding the antisite indicates a significant change in the chemical state and/or the geometrical position of these. In the zoom-in of the antisite in Fig. 10(d), the increased contrast seems smeared out over a large number of the oxygen atoms surrounding the antisite. However, other images [Fig. 9(e)], with the antisite resolved, show that it is only the oxygen atoms nearest the antisite which exhibit an increase in the imaging contrast, reflecting that the O are perturbed by the introduction of Mg on the Al site.

Figure 10(a) shows the simulated frequency detuning vs Z spectroscopy curves for the positively terminated tip apex calculated for 13 relevant sites in the surface unit cell, as indicated on the ball model in Fig. 10(c). For clarity, the spectroscopy curves are divided into three main groups of increasing contrast with labels indicated on the graph and also on top of the ball model in Fig. 10(c). The ball model illustrates the structure of the top two layers of one unit cell containing one antisite (O: red, Al: dark grey, Mg: green). The four spectroscopy curves marked Al_1-Al_3 and anti are all calculated at positions above the aluminum row and exhibit, exactly like in the experiment, the lowest contrast. The larger group marked O_1-O_2 and Mg_1-Mg_4 of spectroscopy curves with intermediate contrast are calculated either above oxygen atoms not neighboring an antisite or at positions in between the oxygen lattice on top of the Mg row in the subsurface layer. Most interestingly, the last group marked $O_{\text{anti-1}}$-$O_{\text{anti-3}}$ of Z spectroscopy curves, which are all calculated above oxygen atoms surrounding the surface antisite, show significantly higher contrast compared to the O_1-O_2, which are oxygen atoms not neighboring an antisite. This is in very good agreement with the experimental NC-AFM images [Fig. 9(a) and corresponding line scan], where these oxygen atoms surrounding an antisite show a significant contrast increase. The spectroscopy curve marked anti possesses by far the darkest contrast, which is in great resemblance with the experimental images of the antisites [see Fig. 10(d)], which are always depicted as a deep hole surrounded by oxygen atoms showing a significant contrast increase.

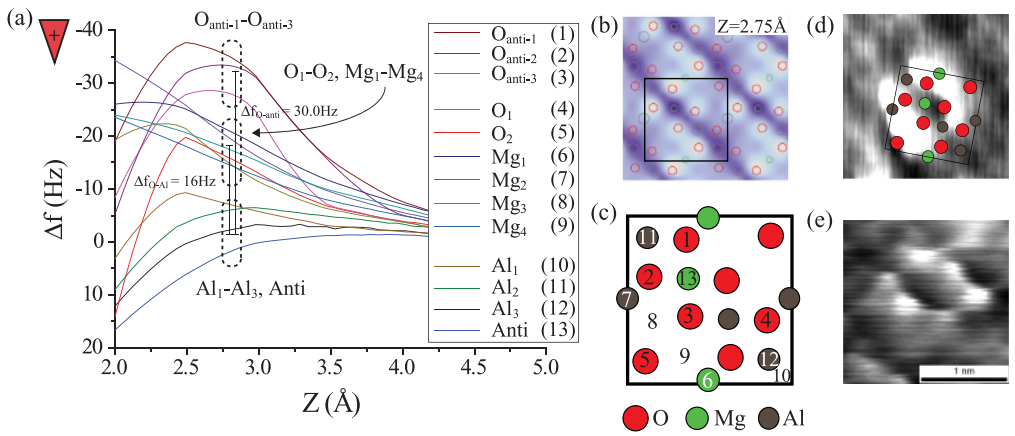

FIG. 10. (Color online) (a) Calculated frequency detuning-vs-distance curves for the positive tip. (b) Simulated image at $Z = 2.75$ Å illustrating how the oxygen atoms neighboring the antisite possess the highest contrast. (c) Ball model indicating the coordinates of the contrast curves in (a). (d) Experimental NC-AFM image zoom-in on an antisite with a ball model on top for guidance. (e) Experimental NC-AFM image with the oxygen atoms surrounding the antisite better resolved.

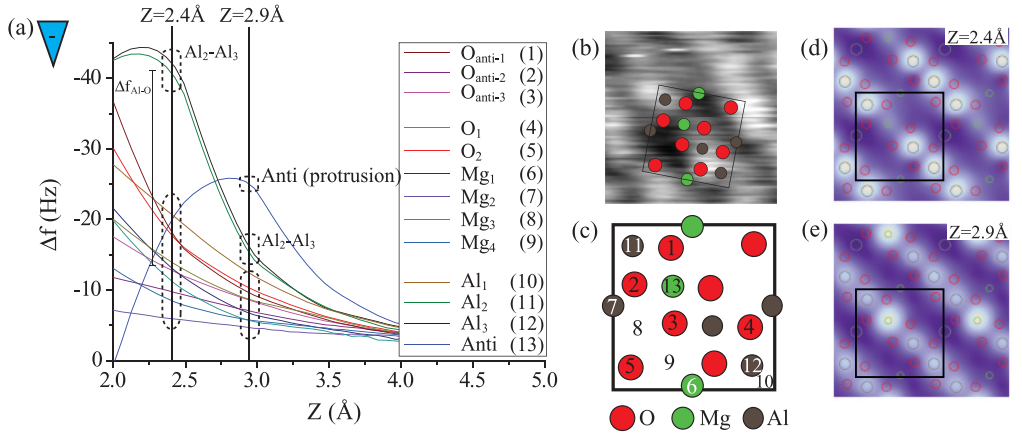

FIG. 11. (Color online) (a) Calculated frequency detuning-vs-distance curves utilizing a negative tip. (b) NC-AFM image zoom-in on an antisite with a ball model on top for guidance. (c) Ball model indicating the coordinates of the contrast curves in (a). (d) Simulated image at $Z = 2.4$ Å illustrating how the antisite is depicted as a hole on the aluminum row. (e) Simulated image at $Z = 2.9$ Å illustrating how the antisite, at larger distances, are imaged as a protrusion on the aluminum row.

Figure 10(b) shows the final simulated image obtained from the spectroscopy curves for a positive tip termination at a distance of $Z = 2.75$ Å, which is representative of the imaging distance of 2.5–3.0 Å that gave the best correspondence between experiment and simulations of the ideal surface in Fig. 4(a). As expected, the simulation shows that the antisites appear as a localized feature superimposed on the well-resolved double-O rows, with an appearance that qualitatively corresponds to the experimental images. The simulation indicates an increased contrast of the oxygen atoms surrounding the antisite (O_{anti-1}-O_{anti-3}), exactly as observed in experiments, although this effect is slightly more pronounced in the experimental images. The corrugation difference between oxygen atoms neighboring an antisite and oxygen atoms not neighboring an antisite is larger in the experimental images [$\Delta f_{O-Al} = 9$ Hz and $\Delta f_{O-anti} = 35$ Hz, see Fig. 9(c)] compared to the simulation [$\Delta f_{O-Al} = 16$ Hz and $\Delta f_{O\text{-}anti} = 30$ Hz, see Fig. 10(a)]. However, this may be attributed to the simplifications related to the tip model. The main features associated with the antisite defects are the same in both simulated and experimental images recorded with a positive tip, i.e. oxygen atoms neighboring an antisite show the highest contrast (most negative Δf at sites O_{anti-1}-O_{anti-3}), and the lowest contrast is located along the aluminum rows (sites marked Al_1-Al_3 and anti) in agreement with experiment.

B. Antisites on $MgAl_2O_4$(100): Negative tip imaging mode

Figure 9(b) shows the experimental NC-AFM image of the surface containing antisite defects imaged with a negative tip. Again, the line scans in Fig. 9(d) show that the antisite defects (dashed circles) are located exactly on the Al lattice. The dashed and solid lines in Fig. 9(d) show a comparison of the corrugation across three Al rows with and without an antisite, respectively. The positions of the line scans are indicated on the NC-AFM image in Fig. 9(b) with similar dashed and solid lines. As seen from the dashed line scan, the Mg atom at the antisite position (Mg'_{Al}) in the middle of the scan exhibits a significant lower contrast compared to normal Al sites. The corrugation is observed to decrease from approximately $\Delta f_{Al\text{-}O} = 2.2$ Hz to $\Delta f_{Al\text{-}anti} = 0.9$ Hz when scanning across the normal Al row and an antisite, respectively. This observation is fully consistent with the qualitative considerations made previously about the antisite contrast in the negative tip mode. The lower charge at the antisite (Mg^{2+} compared to Al^{3+}) causes a lower tip-surface interaction, thereby decreasing the contrast.

Also in this image mode, utilizing the negatively terminated tip apex of the MgO cube, we have calculated Z spectroscopy curves in Fig 11(a). The simulations show the same qualitative features as the experimental images; however, the interpretation of the simulation results should be carried out more carefully here since the contrast at Mg'_{Al} sites (curve marked anti) strongly depends on the imaging distance. The fact that the imaging contrast depends on the tip-surface distance has also been demonstrated in previous work on other oxides materials.[36] However, from the calculated Z spectroscopy curves in Fig. 11(a), it is evident that there are two different imaging regimes depending on the tip-surface distance Z, marked by vertical black lines in the graph. The main difference between the two regimes is the appearance of the Mg'_{Al} antisite, which is depicted as a protrusion on the bright Al row at a far distance ($Z = 2.9$ Å) and depicted as a hole on the bright Al row at a closer distance ($Z = 2.4$ Å). This somewhat counterintuitive effect for a negative tip can be rationalized by a larger outward relaxation of the Mg compared to Al at large tip-surface distances and is therefore mainly a geometric effect induced by the tip-surface forces. To illustrate the distance dependence of the antisite, simulated images have been made from the spectroscopy curves at both distances [Fig. 11(d) and 11(e)], which clearly show this. The simulated Z spectroscopy curves O_{anti-1}-O_{anti-3}, O_1-O_2, Mg_1-Mg_4, and Al_1 always possess the lowest contrast independent of the imaging distance and are representing positions above the oxygen lattice and positions in between the oxygen double rows, as seen from the ball model in Fig. 11(c). The aluminum atoms marked Al_2 and Al_3 will always be revealed with a higher contrast, giving rise to bright Al rows, whereas the

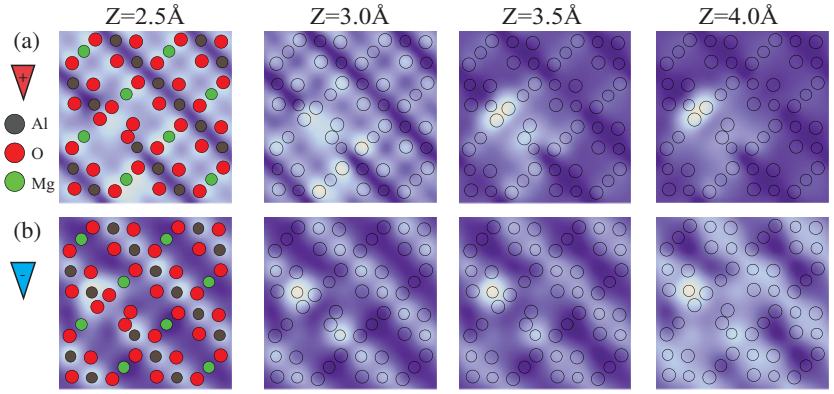

FIG. 12. (Color online) NC-AFM simulations of the O_4-Al_4-O_4-terminated surface containing an Al vacancy utilizing (a) a positive tip and (b) negative tip. In both tip modes, the vacancy is associated with a contrast increase on the aluminum row.

antisite [marked Anti in Fig. 11(a)] will appear as a protrusion or a hole on these bright Al rows, depending on the imaging distance Z.

When reviewing all our NC-AFM images recorded in the negative tip mode, antisites were always depicted as holes on bright rows [as illustrated in the zoom-in Fig. 11(b)]. This is consistent with the simulated images at close tip-surface separations, for instance for $Z = 2.4$ Å [Fig. 11(d)], which is again chosen to reflect the distance that gave best correspondence on the ideal surface in Fig. 6. Also, in this imaging mode, it can therefore be concluded that the antisite model fits the experimental observations very well since the simulations shows the same contrast trends as the NC-AFM images. The contrast regime at $Z = 2.9$ Å [see Fig. 11(a) and 11(e)], where the antisites are depicted as protrusions, was not observed in our experimental images.

C. Al vacancies (V'''_{Al}): NC-AFM simulations

In Figs. 12(a) and 12(b) are included simulated images of the O_4-Al_4-O_4-terminated surface with one surface Al vacancy reflecting the structure in Fig. 1(e). The ball models on top of the simulated images indicate the position of the surface layer O_4-Al_4-O_4 atoms (O: red, Al: dark grey, Mg: green) and the Mg atoms (green/light grey) in the layer below. One image in both modes shows the colored ball model, and in the rest of the simulated images, the color fills are omitted for a better view of the simulated contrast. The four simulated images shown for both tip modes in a range from $Z = 2.5$ to 4.0 Å show that the overall contrast of the Al vacancy does not change significantly with Z. As evident from these images, the Al vacancy is always associated with some increase in contrast regardless the tip termination. Since the Al vacancy (V'''_{Al}) and the antisite (Mg'_{Al}) both act to lower the positive charge on the defect site, some contrast similarity is to be expected.

In the positive tip mode [see Fig. 12(a)], the contrast increases at the vacancy site since the oxygen pair relaxes towards the vacancy site, effectively forming an O_2 molecule, and there is no cation to screen the electrostatic forces from the surrounding oxygen atoms. Although a contrast increase of the oxygen atoms surrounding the vacancy is clearly observed, the contrast fingerprint is not consistent with experiments since the increased brightness has the wrong orientation. In experiments, the increased brightness is always aligned with the oxygen rows, and the Al row always appears with the lowest contrast, defining a 180° symmetry axis of the defect signature. According to simulations, the high brightness appears across a single pair of oxygen atoms that is across the Al row, which is always observed with lowest contrast in experiments. Consequently, according to the simulations in the positive tip mode, it should be straightforward to tell apart a vacancy and an antisite because the vacancy site is associated with a protrusion, whereas the antisite is always depicted as a deep hole on the cation lattice [see Fig. 10(b)]. According to simulations of the negative tip mode [see Fig. 12(b)], the appearance of the Al vacancy and the antisite is quite similar. Here, the Al vacancy site is associated with a hole on the Al row similar to the antisite contrast [see Fig. 11(d)]. However, the two Al atoms on each side of the vacancy site significantly increase in contrast. This contrast increase is attributed to the outwards relaxation of these Al atoms since these are more loosely bound when neighboring a vacancy.

In the experimental images recorded with a positive tip [Fig. 9(a)], distinct protrusions on the Al rows are never observed; on the other hand, the Al rows are always imaged with lowest contrast, and the antisites are always imaged as a hole surrounded by a bright rim of O atoms. Additionally, in the experimental images [Fig. 9(b)], no significant contrast increase is observed on the Al rows surrounding a defect. Consequently, the simulated images in Figs. 12(a) and 12(b) support the conclusion that defects observed on the $MgAl_2O_4$(100) in both Figs. 9(a) and 9(b) are indeed antisite defects and not Al vacancies.

VI. CONCLUSIONS

We have presented a detailed and comprehensive analysis of the effect of tip-apex charge and tip-surface imaging distance in atomic resolved NC-AFM images of the O_4-Al_4-O_4 and 50% Mg terminations of the $MgAl_2O_4$(100) surface. Two distinctively different NC-AFM contrast modes depicting the O or Al lattice of the experimentally observed O_4-Al_4-O_4 termination could be fully reproduced in simulations with a positively or negatively terminated tip apex. By varying the tip-surface distance, some distance-dependent features in both imaging modes were reproduced in the simulations. In the case of a positively charged tip apex, the O lattice is depicted, and at small tip-surface separation, all oxygen atoms are clearly resolved, giving rise to a double-row feature with distances matching the structure model. When the tip-surface distance is increased (by increasing df_{set}), the overall corrugation decreases, and the oxygen atoms are instead resolved in pairs

since the underlying Mg atoms are not able to screen the charge at this larger distance. In the case of a negatively charged tip apex, the Al lattice is depicted as single rows with a periodicity matching the structure model. Again, when scanning the surface at a small tip-surface separation, the individual Al atoms are clearly resolved. However, when increasing the tip-surface distance, the corrugation decreases, and at some point, the individual Al atoms are no longer resolved on the rows, resulting in bright stripes being imaged. Furthermore, the potential surface defects reflecting Al vacancies or Mg-Al antisites on the $MgAl_2O_4(100)$ surface were simulated, and the simulations provided strong support for the existence of stable surface antisites.

Our previous studies showed that hydrogen is expected to adsorb very strongly on the surface and lead to the formation of surface OH groups located on the original O positions.[7] However, no direct evidence of hydrogen could be extracted from the experimentally observed NC-AFM contrast for images obtained with the positive tip. This effect can tentatively be rationalized by a high mobility of hydrogen atoms on the $O_4Al_4O_4$-terminated surface, which smears out the contrast, which would be associated with static H atoms on the O atoms. Preliminary simulations of the effect on the NC-AFM contrast when adding static H to the O_4-Al_4-O_4 shows some change in NC-AFM contrast at adsorption sites, but the complete effect of hydrogen and its influence on the NC-AFM imaging contrast will be addressed in a future paper.[53]

In addition to establishing a robust model of the $MgAl_2O_4(100)$ surface, the experimental and theoretical work acts as a very useful reference for further studies on this surface. In line with previous NC-AFM studies on metal oxides, the tip-surface interactions are found to be of pronounced ionic character, implying that the image contrast is mostly determined by the electrostatic contour of the surface and to a much smaller degree on the actual geometrically appearance.

ACKNOWLEDGMENTS

We acknowledge fruitful discussions with A. Stierle and E. Lundgren. The iNANO Group gratefully acknowledges financial support from the Lundbeck Foundation, Haldor Topsøe A/S, and the European Research Council [ERC Grant No. 239834, "Oxidesynergy" (JVL)].

*jvang@phys.au.dk

[1] R. M. Hazen, D. Papineau, W. B. Leeker, R. T. Downs, J. M. Ferry, T. J. McCoy, D. A. Sverjensky, and H. X. Yang, Am. Miner. **93**, 1693 (2008).

[2] *Metal Oxides—Chemistry and Applications*, edited by J. L. G. Fierro (Taylor and Francis group, Boca Raton, FL, 2006), pp 1–783.

[3] J. R. Rostrup-Nielsen, in *Catalysis - Science and Technology*, edited by J. R. Anderson and M. Boudart (Springer-Verlag, Berlin, 1984), Vol. 5, p. 1.

[4] *Metal Oxide Catalysis*, edited by S. D. Jackson and J.S.J. Hargreaves (Wiley-VCH Verlag GmbH & Co., Weinheim, 2009), pp 1–866.

[5] J. Papavasiliou, G. Avgouropoulos, and T. Ioannides, J. Catal. **251**, 7 (2007).

[6] J. P. Jacobs, A. Maltha, J. G. H. Reintjes, J. Drimal, V. Ponec, and H. H. Brongersma, J. Catal. **147**, 294 (1994).

[7] M. K. Rasmussen, A. S. Foster, B. Hinnemann, F. F. Canova, S. Helveg, K. Meinander, N. M. Martin, J. Knudsen, A. Vlad, E. Lundgren, A. Stierle, F. Besenbacher, and J. V. Lauritsen, Phys. Rev. Lett. **107**, 036102 (2011).

[8] K. E. Sickafus, J. M. Wills, and N. W. Grimes, J. Am. Ceram. Soc. **82**, 3279 (1999).

[9] W. G. Bragg, Philos. Mag. **30**, 305 (1915).

[10] M. J. Davies, S. C. Parker, and G. W. Watson, J. Mater. Chem. **4**, 813 (1994).

[11] C. M. Fang, S. C. Parker, and G. de With, J. Am. Ceram. Soc. **83**, 2082 (2000).

[12] C. M. Fang, G. de With, and S. C. Parker, J. Am. Ceram. Soc. **84**, 1553 (2001).

[13] C. M. Fang, S. C. Parker, and G. de With, Euro Ceramics Vii, Pt 1-3 206-2, 543 (2002).

[14] N. J. van der Laag, C. M. Fang, G. de With, G. A. de Wijs, and H. H. Brongersma, J. Am. Ceram. Soc. **88**, 1544 (2005).

[15] N. J. van der Laag, A. J. M. van Dijk, N. Lousberg, G. de With, and L. Dortmans, J. Am. Ceram. Soc. **88**, 660 (2005).

[16] S. V. Yanina and C. Barry Carter, Surf. Sci. **513**, L402 (2002).

[17] J. V. Lauritsen and M. Reichling, J. Phys. Condes. Matter **22**, 263001 (2010).

[18] E. I. Altman and U. D. Schwarz, Adv. Mater. **22**, 2854 (2010).

[19] C. Barth, A. S. Foster, C. R. Henry, and A. L. Shluger, Adv. Mater. **23**, 477 (2011).

[20] C. Barth and M. Reichling, Nature **414**, 54 (2001).

[21] J. V. Lauritsen, M. C. R. Jensen, K. Venkataramani, B. Hinnemann, S. Helveg, B. S. Clausen, and F. Besenbacher, Phys. Rev. Lett. **103**, 076103 (2009).

[22] J. Wang, A. Howard, R. G. Egdell, J. B. Pethica, and J. S. Foord, Surf. Sci. **515**, 337 (2002).

[23] C. Barth and C. R. Henry, Phys. Rev. Lett. **91**, 196102 (2003).

[24] T. V. Ashworth, C. L. Pang, P. L. Wincott, D. J. Vaughan, and G. Thornton, Appl. Surf. Sci. **210**, 2 (2003).

[25] R. K. Mishra and G. Thomas, J. Appl. Phys. **48**, 4576 (1977).

[26] J. H. Harding, Surf. Sci. **422**, 87 (1999).

[27] C. Noguera, J. Phys. Condens. Matter **12**, R367 (2000).

[28] J. Goniakowski, F. Fabio, and N. Claudine, Rep. Prog. Phys. **71**, 016501 (2008).

[29] C. Barth, A. S. Foster, M. Reichling, and A. L. Shluger, J. Phys.: Condens. Matter **13**, 2061 (2001).

[30] J. V. Lauritsen, A. S. Foster, G. H. Olesen, M. C. Christensen, A. Kühnle, S. Helveg, J. R. Rostrup-Nielsen, B. S. Clausen, M. Reichling, and F. Besenbacher, Nanotechnology **17**, 3436 (2006).

[31] G. Kresse and J. Furthmuller, Phys. Rev. B **54**, 11169 (1996).

[32] G. Kresse and J. Furthmuller, Comput. Mater. Sci. **6**, 15 (1996).

[33] G. Kresse and D. Joubert, Phys. Rev. B **59**, 1758 (1999).

[34] P. E. Blochl, Phys. Rev. B **50**, 17953 (1994).

[35]W. A. Hofer, A. S. Foster, and A. L. Shluger, Rev. Mod. Phys. **75**, 1287 (2003).
[36]G. H. Enevoldsen, A. S. Foster, M. C. Christensen, J. V. Lauritsen, and F. Besenbacher, Phys. Rev. B **76**, 205415 (2007).
[37]R. Bennewitz, A. S. Foster, L. N. Kantorovich, M. Bammerlin, C. Loppacher, S. Schär, M. Guggisberg, E. Meyer, and A. L. Shluger, Phys. Rev. B **62**, 2074 (2000).
[38]R. García and R. Pérez, Surface Science Reports **47**, 197 (2002).
[39]F. F. Canova and A. S. Foster, Nanotechnology **22**, 045702 (2011).
[40]T. Trevethan and L. Kantorovich, Nanotechnology **16**, S79 (2005).
[41]*Noncontact Atomic Force Microscopy*, edited by S. Morita, F. J. Giessibl, and R. Wiesendanger (Springer, Berlin, 2009), pp 1–419.
[42]R. Hoffmann, L. N. Kantorovich, A. Baratoff, H. J. Hug, and H. J. Güntherodt, Phys. Rev. Lett. **92**, 146103 (2004).
[43]A. S. Foster, C. Barth, and C. R. Henry, Phys. Rev. Lett. **102**, 256103 (2009).
[44]A. S. Foster, C. Barth, A. L. Shluger, and M. Reichling, Phys. Rev. Lett. **86**, 2373 (2001).
[45]C. Barth, C. Claeys, and C. R. Henry, Rev. Sci. Instrum. **76**, 083907 (2005).
[46]F. Meducin, S. A. T. Redfern, Y. Le Godec, H. J. Stone, M. G. Tucker, M. T. Dove, and W. G. Marshall, Am. Miner. **89**, 981 (2004).
[47]G. B. Andreozzi, F. Princivalle, H. Skogby, and A. Della Giusta, Am. Miner. **85**, 1164 (2000).
[48]F. A. Kröger and H. J. Vink, *Solid State Physics*, Vol. 3, edited by F. Seitz, D. Turnbull (Academic Press, New York, 1956), p. 273–301.
[49]J. A. Ball, S. T. Murphy, R. W. Grimes, D. Bacorisen, R. Smith, B. P. Uberuaga, and K. E. Sickafus, Solid State Sci. **10**, 717 (2008).
[50]J. A. Ball, M. Pirzada, R. W. Grimes, M. O. Zacate, D. W. Price, and B. P. Uberuaga, J. Phys. Condens. Matter **17**, 7621 (2005).
[51]G. H. Enevoldsen, H. P. Pinto, A. S. Foster, M. C. R. Jensen, W. A. Hofer, B. Hammer, J. V. Lauritsen, and F. Besenbacher, Phys. Rev. Lett. **102**, 136103 (2009).
[52]S. Torbrügge, M. Reichling, A. Ishiyama, S. Morita, and O. Custance, Phys. Rev. Lett. **99**, 056101 (2007).
[53]M. K. Rasmussen, A. S. Foster, F. F. Canova, B. Hinnemann, S. Helveg, K. Meinander, F. Besenbacher, and J. V. Lauritsen (2011) (unpublished).